

Extremes, intermittency and time reversibility of atmospheric turbulence at the cross-over from production to inertial scales

E. Zorzetto,^{1, a)} A.D. Bragg,^{2, b)} and G. Katul^{3, c)}

¹⁾*Division of Earth and Ocean Sciences, Nicholas School of the Environment,
Duke University, Durham, North Carolina 27708, USA*

²⁾*Department of Civil and Environmental Engineering, Duke University, Durham,
North Carolina 27708, USA*

³⁾*Nicholas School of the Environment, Duke University, Durham,
North Carolina 27708, USA*

(Dated: 13 May 2022)

The effects of mechanical generation of turbulent kinetic energy and buoyancy forces on the statistics of air temperature and velocity increments are experimentally investigated at the cross over from production to inertial range scales. The ratio of an approximated mechanical to buoyant production (or destruction) of turbulent kinetic energy can be used to form a dimensionless stability parameter ζ that classifies the state of the atmosphere as common in many atmospheric surface layer studies. Here we assess how ζ affects the scale-wise evolution of the probability of extreme air temperature excursions, their asymmetry and time reversibility. The analysis makes use of high frequency velocity and air temperature time series measurements collected at $z=5$ m above a grass surface at very large Reynolds numbers $Re = u_* z / \nu > 1 \times 10^5$ (u_* is the friction velocity and ν is the kinematic viscosity of air). Using conventional higher-order structure functions, temperature exhibits larger intermittency and wider multifractality when compared to the longitudinal velocity component, consistent with laboratory studies and simulations conducted at lower Re . Moreover, deviations from the classical Kolmogorov scaling for the longitudinal velocity are shown to be reasonably described by the She-Leveque vortex filament model that has no 'tunable' parameters and is independent of ζ . The work demonstrates that external boundary conditions, and in particular the magnitude and sign of the sensible heat flux, have a significant impact on temperature advection-diffusion dynamics within the inertial range. In particular, atmospheric stability affects both the buildup of intermittency and the persistent asymmetry and time irreversibility observed in the first two decades of inertial sub-range scales.

Keywords: Atmospheric Boundary Layer, Extreme Value Statistics, Turbulence, Time-reversibility, Ramp-Cliff patterns

^{a)}Electronic mail: enrico.zorzetto@duke.edu.

^{b)}Electronic mail: andrew.bragg@duke.edu.

^{c)}Electronic mail: gaby@duke.edu.

I. INTRODUCTION

Turbulence in fluids is prototypical of spatially extended nonlinear dissipative systems characterized by large fluctuations that are active over wide ranging scales¹. Scalar turbulence is by no means an exception to this description. Scalar turbulence share many phenomenological parallels with the much studied turbulent velocity fluctuations, especially in the inertial subrange. However, scalar turbulence also exhibits distinctive large- and fine-scaled temporal patterns (e.g. ramp-cliff) that are usually weak or all together absent from their component-wise turbulent velocity counterparts²⁻⁴. This finding is particularly true in the atmospheric surface layer (ASL)^{5,6}, a layer within the atmospheric boundary layer (ABL) that is sufficiently far above roughness elements but not too far from the ground to be directly impacted by the Coriolis force. In the ASL, the Reynolds number $Re = u_* z / \nu$ can readily exceed 10^5 , where z is the distance above the ground surface, u_* is the friction velocity related to the kinematic turbulent stress, and ν is the kinematic viscosity of air. A direct consequence of this large Re is a wide separation between scales over which turbulent kinetic energy (k) is produced and dissipated. In the absence of thermal stratification, k is produced at scales commensurate with z ; however, the action of fluid viscosity responsible for the dissipation of k occurs at scales commensurate to or smaller than the Kolmogorov microscale $\eta_K = (\nu^3 / \langle \epsilon \rangle)^{1/4}$, where $\langle \epsilon \rangle$ is the mean turbulent kinetic energy dissipation rate that is proportional to u_*^3 / z for a neutrally stratified ASL⁶. These estimates of $\langle \epsilon \rangle$ and η_K result in $z / \eta_K \sim Re^{3/4} > 5000$ in the ASL, which is rarely achieved in direct numerical simulations or laboratory studies. Embedded in this wide ranging scale separation is the inertial subrange⁷, where self similar scaling of velocity and air temperature structure functions is expected to hold for eddy sizes much larger than η_K but much smaller than z . Integral scales or scales comparable to z are directly influenced by boundary conditions imposed on the flow including surface heating (or cooling) in the ASL, whereas small scales (e.g. η_K) may attain universality and local isotropy after a large number of cascading steps away from the energy injection scales.

Much attention has been historically dedicated to the inertial subrange and the subsequent cross-over to the viscous or molecular regimes precisely because of the possible universal character of turbulence at such fine scales^{4,8-12}. However, it is now accepted that some coupling between small and large scales exists, especially for passive scalars^{3,4,13}, that

act to enhance intermittency buildup across scales and distort any universal behavior by injecting the effects of the boundary conditions (or the k generation mechanism). Along similar lines of inquiry, it has been conjectured that the presence of coherent ramp-cliff patterns in concentration (or temperature) time series are responsible, to some degree, for this coupling⁴. Ramp-cliff structures are characterized by local intense scalar gradients separated by large quiescent regions. The presence of ramp-cliff structures in scalar time series has been shown to break locality of eddy interactions and determine some departures from small scale isotropy.

Sweep-ejection dynamics connected to the presence of ramps are likely to play a major role in observed extreme value statistics, as shown e.g., for Lagrangian velocity sequences in plant canopy turbulence¹⁴. Moreover, ramps are asymmetric and produce non-zero odd ordered structure functions, sharing striking resemblance with flight-crash events recently reported for the turbulent kinetic energy of Lagrangian particles¹⁵. Even though ramps have been extensively observed experimentally², studied as surface renewal processes¹³, and from a Lagrangian perspective^{3,16}, a unified picture on their effects on inertial scales statistics remains lacking and motivates the work here.

Our main objective is to investigate two questions about scalar turbulence at scales spanning production to inertial subranges: How do ramp-cliff patterns modify (i) the probability of extreme scalar concentration excursions and its corollary intermittency buildup, and (ii) symmetry and time reversibility of scalar turbulence. These two questions are explored for differing turbulent energy injection mechanisms (mechanical and buoyancy forces) in the ASL. Here we focus on the production-to-inertial scales instead of the usual inertial to viscous ranges for the following reasons. First, any cross-scale coupling with ramp-cliff patterns is likely to be sensed at large scales commensurate with the ramp durations. Second, these scales are deemed most relevant when constructing sub-grid scale models for improving Large Eddy Simulations^{17–20}. Third, these scales encode much of the scalar variance that is needed when deriving phenomenological theories for the bulk flow properties based on the spectral shapes of the turbulent velocity and air temperature^{21–25}, especially for the ASL.

To achieve the study objectives, high frequency measurements of the three velocity components and air temperature fluctuations in the ASL are used to explore flow statistics at the transition from production to inertial scales. In particular, the focus is on the first two decades dominated by approximate inertial subrange effects, where the transition from the

large eddies to the universal equilibrium or inertial range occurs. The statistical properties of temperature increments within this range of scales is examined with the goal of addressing to what extent the tail properties (and thus the probability of extreme events) at fine scales still carry signatures from the production ranges and in particular of large coherent structures (such as ramp-cliff). The experiments here spanned several atmospheric stability regimes that dictate to what degree turbulent kinetic energy is mechanically or buoyantly generated (or dissipated) depending on surface heating (or cooling) and the turbulent shear stress near the ground²⁶.

II. THEORY

A. Overview of ASL similarity at large- and small-scales

The k budget for a stationary and planar homogeneous flow in the absence of subsidence is given by

$$\frac{\partial k}{\partial t} = 0 = -\overline{u'w'}\frac{dU}{dz} + \beta_o g \overline{w'T'} + P_D + T_T - \epsilon, \quad (1)$$

where $k = (\overline{u'^2} + \overline{v'^2} + \overline{w'^2})/2$, u' , v' , and w' are the turbulent velocity components along the mean wind (or x), lateral (or y), and vertical (or z) directions, respectively, t is time, and the five terms on the right-hand side of equation 1 are mechanical production, buoyant production (or destruction), pressure transport, turbulent transport of k , and viscous dissipation of k , respectively, β_o is the thermal expansion coefficient for gases ($\beta_o = 1/T$, T is air temperature here), g is the gravitational acceleration, $-\overline{u'w'} = u_*^2$ is the turbulent kinematic shear stress near the surface, and $\overline{w'T'}$ is the kinematic sensible heat flux from (or to) the surface. When $\overline{w'T'} > 0$, buoyancy is responsible for the generation of k and the ASL is classified as unstable. When $\overline{w'T'} < 0$, the ASL is classified as stable and buoyancy acts to diminish the mechanical production of k . The relative significance of the mechanical production to the buoyancy generation (or destruction) may be expressed as

$$-\overline{u'w'}\frac{dU}{dz} + \beta_o g \overline{w'T'} = \frac{u_*^3}{\kappa z} \left[\phi_m(\zeta) + \frac{\kappa z \beta_o g \overline{w'T'}}{u_*^3} \right] = \frac{u_*^3}{\kappa z} [\phi_m(\zeta) - \zeta], \quad (2)$$

where

$$\frac{u_*}{\kappa z} \frac{dU}{dz} = \phi_m(\zeta), \zeta = \frac{z}{L}, L = -\frac{u_*^3}{\kappa g \beta_o \overline{w'T'}}, \quad (3)$$

and $\phi_m(\zeta)$ is known as a stability correction function reflecting the effects of thermal stratification on the mean velocity gradient ($\phi_m(0) = 1$ recovers the von Karman-Prandtl log-law), $\kappa \approx 0.4$ is the von Karman constant, and L is known as the Obukhov length as described by the Monin and Obukhov similarity theory²⁶. The physical interpretation of L is that it is the height at which mechanical production balances the buoyant production or destruction when $\phi_m(\zeta)$ does not deviate appreciably from unity. For a neutrally stratified ASL flow, $|L| \rightarrow \infty$ and $|\zeta| \rightarrow 0$.

Several bulk flow statistics in the ASL can be reasonably described by the aforementioned Monin-Obukhov similarity theory, including the mean air temperature gradient dT/dz and the air temperature variance $\overline{T'^2}$, both varying with ζ when normalized by a temperature scale $T_* = -\overline{w'T'}/u_*$. However, the statistics of large-scale features within the temperature time series traces such as the statistics of ramp-cliff patterns do not scale with z . For starters, the ramp characteristic dimension is generally larger than z and their duration exceeds $(\kappa z \phi_m(\zeta)^{-1})u_*^{-1}$. Ramps have been observed within canopies, near the canopy atmosphere interface, and other types of flows as reviewed elsewhere^{4,13}. However, z/L does indirectly impact several features of the ramp-pattern in air temperature traces sampled within the ASL. For example, in stably stratified ASL flows, the temperature ramps appear 'inverted' when compared to their near-neutral counterparts. The amplitudes and durations of ramps can increase with increasing instability due to weaker shearing and intense buoyant updrafts^{27,28}.

At small scales associated with the inertial subrange, the velocity and temperature second-order structure functions are commonly described by the Kolmogorov 1941 (K41) theory⁷ given as

$$S_u^2(r) = \overline{[\Delta u(r)]^2} = 4C_{o,u}(\langle \epsilon \rangle r)^{2/3}, \quad (4)$$

$$S_w^2(r) = \overline{[\Delta w(r)]^2} = 4C_{o,w}(\langle \epsilon \rangle r)^{2/3}, \quad (5)$$

$$S_T^2(r) = \overline{[\Delta T(r)]^2} = 4C_{o,T}\langle \epsilon_T \rangle \langle \epsilon \rangle^{-1/3} r^{2/3}, \quad (6)$$

where $\Delta u(r) = u(x+r) - u(x)$, $\Delta w(r) = w(x+r) - w(x)$, and $\Delta T(r) = T(x+r) - T(x)$, are the velocity and temperature increments at separation distance (or scale) r , $\langle \epsilon \rangle$ and $\langle \epsilon_T \rangle$ are the k and temperature variance dissipation rates, respectively, $C_{o,u}$ and $C_{o,w}$ are

the Kolmogorov constants for the longitudinal and vertical velocity components, and $C_{o,T}$ is the Kolmogorov-Obukhov-Corrsin (KOC) constant. These scaling laws, obtained under the assumptions of similarity and local isotropy, appear to hold reasonably in the ASL for scales smaller than $z/2^{29}$. Moreover, the normalized third order structure functions

$$S(r) = \frac{S_u^3}{(S_u^2)^{3/2}} = \frac{\langle \Delta u(r)^3 \rangle}{\langle \Delta u(r)^2 \rangle^{3/2}} \quad (7)$$

and

$$F(r) = \frac{S_{TTu}^3}{S_T^2 [S_u^2]^{1/2}} = \frac{\langle \Delta u(r) \Delta T(r)^2 \rangle}{\langle \Delta T(r)^2 \rangle \langle \Delta u(r)^2 \rangle^{1/2}} \quad (8)$$

must be constant to recover K41 predictions for S_u^2 and S_T^2 in the inertial range³⁰.

However, relevant deviations from K41 scaling have been reported for higher order structure functions, especially for the scalar fluctuations. These deviations arise as (i) Eq. (6) does not account for intermittency related to spatial variability of the actual ϵ and ϵ_T , and (ii) the hypothesis of local isotropy might not hold for scalars due to non-local interactions across scales³¹. A signature of the latter is the large structure skewness for temperature determined by ramp structures^{4,29}. Many models, starting from Kolmogorov's log-normal dissipation rate refinement³², seek to relax some of the restrictive assumptions of K41 so as to explain the anomalous scaling observed in higher order moments. For scalars, these corrections are commonly expressed as

$$S_T^n = C_n (\epsilon r)^{n/3} (r/L_I)^{\zeta'_n - n/3} \quad (9)$$

where the exponent ζ'_n implies a scaling different from K41 that depends on the moment order n . The presence of an integral time scale L_I suggests an explicit dependence on large scale eddy motion within the inertial subrange. One estimate of L_I may be derived from the integral time scale of the flow given by

$$L_I = U \cdot I_w = U \cdot \int_0^\infty \rho_w(\tau_0) d\tau_0, \quad (10)$$

where $\rho_w(\tau_0)$ is the vertical velocity autocorrelation function and τ_0 is the time lag. Here, I_w is presumed to be the most restrictive scale given that w' is the flow variable most impacted by the presence of the boundary.

The statistics of air temperature increments across scales (τ_0/I_w) for different ζ conditions are explored with a lens on two primary features: buildup of heavy tails and destruction

of asymmetry originating from ramp-cliff structures at the cross-over from $\tau_0/I_w > 1$ to $\tau_0/I_w \approx 0.1$. Because changes in ζ do result in changes in I_w , the time (or space) lags are presented in dimensionless form as $\tau = \tau_0/I_w$.

B. Probabilistic description of intermittency

A number of models have been proposed to capture the effects of intermittency on the flow statistics in the inertial range of scales (e.g., lognormal, bi- and multi-fractals - beta model, log-stable, She-Leveque vortex filaments, etc) and documented by several ASL experiments^{33,34}. Common to all these models is the hypothesis of local isotropy and the accounting for uneven distribution of eddy activity in the space/time domain, which explains the anomalous scaling of the higher order even structure functions.

Here, a statistical description of scalar increments is used to fingerprint large-scale signatures across scales τ for different ζ . If such fingerprints exist, the dissipation rates ϵ and ϵ_T need not be sufficient to describe all aspects of the inertial range statistics. The one-time probability density function (pdf) of the increments of a flow variable Δs , with $\Delta s = \Delta u(\tau), \Delta w(\tau), \Delta T(\tau)$ at a given dimensionless scale τ , can be expressed as³⁵

$$p(\Delta s) = \frac{N}{q_o(\Delta s)} \exp \int_0^{\Delta s} \frac{r_o(\Delta s')}{q_o(\Delta s')} d\Delta s'. \quad (11)$$

This expression is exact when Δs are realizations of a stationary stochastic process $S(t)$ under the condition $p(\Delta s) \rightarrow 0$ as $\Delta s \rightarrow \infty$. Here $q_o(\Delta s) = \langle \dot{S}^2 | \Delta s \rangle / \langle \dot{S}^2 \rangle$ and $r_o(\Delta s) = \langle \ddot{S} | \Delta s \rangle / \langle \dot{S}^2 \rangle$ are the normalized averages of the first and second order conditional derivatives of the process $S(t)$, and N is a normalization constant. Eq. (11) generalizes previous results obtained by Sinai and Yakhot³⁶ and Ching³⁷ for the pdf of temperature fluctuations and their increments, where the term $r_o(\Delta s)$ was linear ($r_o(\Delta s) = -\Delta s$). Eq. (11), while derived for a twice-differentiable process, can be interpreted as the steady-state solution of a Fokker Planck (FP) equation with $p(\Delta s)$ vanishing at infinite boundaries, with drift and diffusion coefficient equal to r_0 and q_0 respectively^{38,39}.

Although Eq. (11) can be directly computed from an observed time series, the estimation of the conditional derivatives in $q_o(\Delta s)$ and $r_o(\Delta s)$ becomes inevitably uncertain as Δs approaches the tails of the pdf. However, a number of parametric distributions commonly used in statistical mechanics arise as particular cases of Eq. (11) when $r_o(\Delta s) = -\Delta s$,

such as Gaussian (q_o constant), power-laws ($q_o(\Delta s) \sim \Delta s^2$) and stretched exponentials ($q_o(\Delta s) \sim \Delta s^a, 0 < a < 2$). To facilitate estimation and comparisons with data, two different parametric models for the tails of Eq. (11) are here adopted: a Stretched Exponential (SE) and a Q-Gaussian distribution (QG). The first arises from multiplicative processes of normal-distributed random variates⁴⁰, while the second maximizes a generalized measure of information entropy proposed by Tsallis^{41–43}. While QG does not have a clear physical basis in the context of turbulent flows⁴⁴, it has been widely used in the analysis of turbulence simulations and data^{13,45–48}. We employ these two models to infer tail behavior as well as to test the independence of our findings from the particular parametric distribution used to characterize $p(\Delta s)$. The QG and SE pdfs are given as

$$p_{QG}(\Delta s) = N(q) \cdot \left(1 + (q - 1) \frac{\Delta s^2}{2\psi^2} \right)^{\frac{1}{1-q}}, \quad (12)$$

$$p_{SE}(\Delta s) = \frac{\eta}{\lambda} \left(\frac{\Delta s}{\lambda} \right)^{\eta-1} \cdot \exp \left(- \frac{\Delta s}{\lambda} \right)^{\eta}. \quad (13)$$

Both pdf models have two degrees of freedom corresponding to a scale (ψ, λ) and shape (η, q) parameter. We adopt the (symmetric) QG model and the SE fitted separately to right and left tails of $p(\Delta T)$.

C. Probabilistic description of asymmetry and irreversibility across scales

The presence of ramp-cliff structures has been conjectured to result in non local interactions of different size eddies within the inertial subrange⁴. This non-locality affects both even and odd moments of higher order. A statistical framework to investigate the effects of ramps on the asymmetric nature of velocity and scalar increments for different atmospheric stability classes is now discussed. Sharp edges associated with cliffs might directly inject scalar variance at much smaller scales and thus alter the magnitude and sign of odd order moments within the inertial range (depending on z/L). In particular, this effect can be measured by the skewness of the scalar increments $S_T^3 = \langle \Delta T(\tau)^3 \rangle / \langle \Delta T(\tau)^2 \rangle^{3/2}$.

However, a further signature of ramp-cliff structures is that increments $\Delta T(\tau)$ may exhibit a time directional (or 'irreversible') behavior. Time series reversibility implies that the trajectories of a stationary process Θ_t exhibit the same statistical properties when considered forward or backward in time. In particular, for a reversible time series the n-points joint pdf

of $(\Theta_1, \Theta_2, \dots, \Theta_n)$ is equal to the joint pdf of the reversed sequence $(\Theta_n, \Theta_{n-1}, \dots, \Theta_1)$ for every n . While testing this general definition of reversibility would require perfect knowledge of the phase space trajectories, a weaker definition is the so called lag-reversibility. This condition only requires the two-points pdfs to be equal: $f_{\Theta_t, \Theta_{t+\tau}}(\Theta_1, \Theta_2) = f_{\Theta_{t+\tau}, \Theta_t}(\Theta_2, \Theta_1)$. While this definition is less general, it still provides a necessary condition for testing the more general time reversibility. Moreover, it is consistent with the traditional descriptions of turbulence that are primarily based on two-point statistics. Lag reversibility implies that⁴⁹

$$R_\tau = \text{corr}(\Theta_t^2, \Theta_{t+\tau}) - \text{corr}(\Theta_t, \Theta_{t+\tau}^2) = 0. \quad (14)$$

This condition can be directly tested across different τ and ζ using conventional correlation analysis.

A second test for reversibility of scalar trajectories is here performed based on the Kullback-Leibner measure, a form of relative entropy that determines the average distance between the entire pdf of forward and backward trajectories^{39,50,51}. Again, the analysis here is restricted to the inspection of lag-reversibility ($n = 2$) across scales τ . In such a restricted form, this measure reduces to

$$\langle Z_\tau \rangle = \int_{\Omega_\Theta} p(\Theta) d\Theta \int_{\Omega_{\Theta'_\tau}} p(\Theta'_\tau | \Theta) \cdot \log \frac{p(\Theta'_\tau | \Theta)}{p(-\Theta'_\tau | \Theta)} d\Theta'_\tau, \quad (15)$$

where $\Theta'_\tau = \Delta\Theta(\tau)/\tau$, and the domains of integration Ω_Θ and $\Omega_{\Theta'_\tau}$ correspond to the populations of the random variables Θ and Θ'_τ respectively. Eq. (15) determines, at each dimensionless scale τ , the average distance between the probability of the transition $\Delta\Theta(\tau)$ and its inverse, at every given level Θ .

A statistical mechanics interpretation of Eq. (15) would imply that for a system in non-equilibrium steady state, the *Fluctuation Theorem* must hold so that

$$\log \frac{p(-Z_\tau)}{p(Z_\tau)} = -Z_\tau \quad (16)$$

for the variable Z_τ computed at some level Θ

$$Z_\tau(\Theta) = \log \frac{p(\Theta'_\tau | \Theta)}{p(-\Theta'_\tau | \Theta)}. \quad (17)$$

Note here the usage of conditional probabilities instead of their unconditional forms employed in recent flight-crash studies of Lagrangian fluid particles¹⁵ that also made use of

Fluctuation Theorem and time-reversibility. Eq. (15) has been shown to have general validity⁵¹ independent of the underlying dynamics or statistical-mechanics interpretations, when considering conditional statistics.

III. DATA AND METHODS

The three velocity components and air temperature measurements were sampled at 56 Hz using an ultra-sonic anemometer positioned at $z = 5.2$ m above a grass-covered surface at the Blackwood Division of the Duke Forest, near Durham, North Carolina, USA. The anemometer samples the air velocity in three non-orthogonal directions by transmitting sonic waves in opposite directions and measuring their travel times along a fixed 0.15 m path length. Temperature fluctuations are then computed from measured fluctuations in the speed of sound assuming air is an ideal gas. The experiment resulted in 123 runs, each run having a duration of 19.5 minutes (65536 data points at 56Hz), covering a range of different atmospheric stability conditions²⁹. The assumption of stationarity is necessary so as to (i) decompose the flow variables into a mean and fluctuating part, (ii) adopt Eqs. (11) and (15) so as to describe intermittency and time irreversibility respectively, (iii) compute integral time scales needed in delineating the transition from production to inertial. To test the dataset for stationarity, we employ the second order structure functions of velocity components (u, w) and air temperature T . Runs were included only if the slope of $S_s^2 = \langle [s(t + \tau) - s(t)]^2 \rangle$ for time delays larger than about 9 minutes (30000 sample points) was smaller than a fixed value (0.01). Only 34 runs were retained based on this strict stationarity criterion. Their corresponding second order structure functions for w and T are featured in Fig. 1. As expected, structure functions exhibit an approximate $2/3$ scaling at fine scales and transition to a constant value as the autocorrelation weakens at large separation distances.

As earlier noted, the most restrictive (i.e. smallest) integral timescale is I_w associated with the vertical velocity w due to ground effects. We assume that this timescale characterizes the transition from production to inertial ranges for all three flow variables u, w, T . Eq (10) is here evaluated by integrating $\rho_w(\tau)$ up to the first zero crossing so as to avoid the effects of low frequency oscillations. Figure 1 illustrates the integral time scales of w and T as a function of z/L , where the aforementioned integral time scales are normalized by

the mean vorticity time scale $dU/dz = \phi_m(\zeta)u_*(\kappa_v z)^{-1}$. It is clear that such normalized I_w is approximately constant across stability regimes and suggests I_w to be proportional to the duration of vortices most efficient at transporting momentum to the ground for all ζ . Conversely, the temperature integral time scale is much longer than I_w for near-neutral conditions and only approaches I_w for strongly unstable conditions.

A known limitation of sonic anemometry is the presence of distortions at high frequencies due to instrument path-averaging. For this reason, the smallest scale considered in the analysis is $0.05 \cdot I_w$, which corresponds to a minimum travel path of 30cm (or twice the sonic anemometer path length). Taylor’s frozen turbulence hypothesis⁵² ($r = -\bar{U}t$) was employed to convert values of τ to separation distances r within the inertial subrange even though the turbulent intensity σ_u/U is not small as shown in Table I. For this reason, we adopt the dimensionless lag τ for analysis and presentation. The τ can be interpreted as temporal or spatial noting that distortions due to the use of Taylor’s hypothesis impact similarly the numerator and denominator.

To compare the data sets here with laboratory studies, a number of statistics were computed and presented. The validity of Obukhov’s constant skewness hypothesis was tested for u in Figure 2, which reports the values of the third order structure functions Eqs. (7) and (8) evaluated at the onset of the inertial subrange delineated by the w time series. Both are approximately constant for scales smaller than I_w . While comparison with experiments shows good agreement for $S(\tau) \simeq -0.25$, $F(\tau)$ is systematically smaller than its anticipated value²⁹ (-0.4) for all ζ .

Inspection of scaling exponents ζ'_n in Eq. (9) for u, w, T confirms that K41 predictions significantly overestimate scaling exponents for structure functions of order higher than 2, as shown in figure 3(A). The scaling exponents obtained for the scalar T show reasonable agreement with previous experimental results (Fig. 3(B)), with values systematically lower than predicted by the Kraichnan model in the limiting case of time-uncorrelated velocity field⁵³.

For every run, ζ was computed using Eq. (3) and then employed to classify the ASL stability condition. Most of the runs in the dataset are unstable with a wide range of $|z/L|$, while only 4 runs are characterized by $\zeta > 0$. To ensure a balanced statistical design, two stability classes are selected with the same number of runs (8) in each class: strongly unstable ($|z/L| > 0.5$) and near neutral runs ($|z/L| < 0.072$). A summary of the bulk flow

properties for these runs are featured in Table (I).

In the analysis, each flow variable s ($s = u, w, T$) is normalized to zero-mean and unit-variance (labeled as s_n). Then, at scale τ , a time series of $\Delta s(\tau) = s_n(t + \tau) - s_n(t)$ is constructed and again normalized to have unit variance.

For illustration purposes, Fig. 4 shows sequences of fluctuations u', w', T' extracted from runs in unstable and stable atmospheric regimes. In the first case, temperature fluctuations clearly exhibit ramp-cliff structures occurring with time scales larger than I_w . In the stable/near neutral case, large scale scalar structure are still present even though their structure is qualitatively different from the unstable case, and may include inverted ramp structures as in Fig. 4(B) when $\overline{w'T'} < 0$.

To test the effects of these coherent structures on inertial subrange statistics, and in particular to isolate the effect of temperature ramps on intermittency and asymmetry, synthetic time series are used and are constructed as follows. First, a phase-randomization of the original temperature records⁵⁴ is performed by preserving the amplitudes of the Fourier coefficients while destroying coherent patterns encoded in the phase angle. A synthetic sawtooth time series is then superimposed on the time series obtained by phase-randomization. Here a coefficient α measures the relative weight of the ramps with respect to the phase-randomized sequence. This combination yields realizations of a renewal process (see Fig. 4(C) for a representative example with $\alpha = 0.5$) that is unconnected with Navier-Stokes scalar turbulence, but mimics sweep-ejection dynamics¹³. Synthetic ramps are here generated with exponentially distributed durations and with a mean duration set to a multiple of the integral time scale ($2 \cdot I_w$ in Figure 4(C)). The resulting time series is again normalized to have zero mean and unit variance.

Eq. (15) was computed by integrating the relative entropy over the joint frequency distribution of normalized temperature fluctuations and their increments at each scale τ . Following⁵¹, we use a coarse binning for estimating the joint pdf $p(T'(\tau), T)$ and assume that only finite probability ratios contribute to $\langle Z_\tau \rangle$. To check the consistency of this approach, calculations of Eq. (15) were repeated using a phase space reconstruction technique based on embedding sequences $(T_t, T_{t+\tau})$ with delay time τ and embedding dimension 2, which confirmed the validity of our approach (results not shown).

TABLE I: Bulk flow properties for the runs belonging to the two broad atmospheric stability classes: unstable runs ($\zeta < -0.5$) and near neutral runs ($|\zeta| < 0.072$). The table reports the atmospheric stability parameter ζ , the Obukhov length L [m], the sensible heat flux ($\rho C_p \overline{w'T'}$ [$W m^{-2}$] (where ρ is the mean air density and C_p is the specific heat capacity of dry air at constant pressure), the mean air temperature T [$^{\circ}C$] and velocity U [m/s], and the integral time scale for w [s], the turbulent intensity σ_u/U , the temperature standard deviation σ_T [$^{\circ}C$], and vertical velocity standard deviation σ_w [m/s].

Run	ζ	L	H	T	U	I_w	σ_u/U	u^*	σ_T	σ_w
1	-11.56	-0.4	93.2	33.9	2.1	2.62	0.44	0.08	0.48	0.40
2	-1.31	-4.0	121.6	26.9	1.0	7.58	0.72	0.17	0.54	0.30
3	-0.89	-5.8	73.1	27.8	0.5	6.62	0.91	0.16	0.37	0.30
4	-0.81	-6.4	79.9	32.7	0.7	5.75	1.05	0.17	0.61	0.29
5	-0.80	-6.5	138.1	27.4	0.8	8.18	0.48	0.21	0.57	0.31
6	-0.67	-7.7	149.8	31.4	0.9	11.64	1.04	0.23	0.63	0.38
7	-0.59	-8.8	118.1	34.8	1.5	3.43	0.71	0.22	0.58	0.34
8	-0.52	-10.0	85.4	32.5	2.1	1.74	0.37	0.21	0.44	0.37
9	-0.45	-11.5	78.6	31.7	1.1	7.44	0.61	0.21	0.43	0.30
10	-0.44	-11.7	110.7	31.9	1.2	5.89	0.65	0.24	0.49	0.37
11	-0.44	-11.8	39.4	34.4	1.3	3.19	0.45	0.17	0.32	0.29
12	-0.40	-13.0	36.6	34.1	1.7	2.30	0.39	0.17	0.37	0.28
13	-0.37	-14.0	65.1	25.2	1.6	2.91	0.39	0.21	0.35	0.27
14	-0.33	-15.6	48.0	28.9	1.4	2.58	0.41	0.20	0.27	0.30
15	-0.33	-15.8	4.8	33.4	1.6	1.59	0.35	0.09	0.09	0.23
16	-0.29	-18.2	115.2	32.1	2.7	2.16	0.37	0.28	0.44	0.47
17	-0.28	-18.5	136.2	29.2	0.9	6.88	1.11	0.30	0.56	0.37
18	-0.27	-19.1	108.6	30.5	1.7	3.56	0.62	0.28	0.54	0.34

Run	ζ	L	H	T	U	I_w	σ_u/U	u^*	σ_T	σ_w
19	-0.17	-29.7	70.5	29.5	2.6	2.22	0.29	0.28	0.36	0.42
20	-0.15	-33.8	63.2	32.9	2.2	2.97	0.39	0.28	0.36	0.40
21	-0.14	-37.9	30.9	34.2	1.6	4.17	0.49	0.23	0.34	0.32
22	-0.12	-44.4	118.6	31.0	2.6	3.78	0.42	0.38	0.49	0.42
23	-0.09	-56.5	26.7	33.9	1.9	3.39	0.31	0.25	0.15	0.31
24	-0.08	-61.7	49.7	31.7	2.0	3.50	0.41	0.31	0.27	0.39
25	-0.08	-65.1	17.6	34.0	2.2	3.22	0.29	0.23	0.13	0.31
26	-0.07	-72.5	28.8	31.5	1.8	2.71	0.41	0.28	0.29	0.30
27	-0.04	-126.2	45.1	31.0	4.3	1.21	0.33	0.39	0.35	0.71
28	-0.03	-171.8	3.9	31.3	1.7	3.18	0.39	0.19	0.15	0.30
29	-0.02	-261.4	46.1	31.2	3.8	1.37	0.39	0.50	0.23	0.72
30	-0.02	-304.3	47.1	29.4	5.0	0.84	0.31	0.53	0.21	0.80
31	0.002	2397.4	-0.4	31.2	1.9	1.94	0.44	0.22	0.69	0.32
32	0.01	525.5	-1.3	32.9	0.9	3.00	0.51	0.19	0.18	0.23
33	0.05	93.8	-20.7	29.8	2.6	1.52	0.30	0.27	0.23	0.39
34	0.07	71.4	-14.2	30.4	1.9	2.18	0.37	0.22	0.25	0.28

RESULTS

The main questions to be addressed require determination of the scale-wise evolution of (i) the probability of extreme scalar concentration excursions and concomitant intermittency buildup, and (ii) symmetry and time reversibility. These two questions are explored using the data sets here for stable, near neutral and unstable ASL runs.

A. Probabilistic description of intermittency across scales

The empirical pdfs of velocity and air temperature increments ($\Delta s = \Delta u, \Delta w, \Delta T$) for runs in the near-neutral ($|\zeta| < 0.072$) and strongly unstable ($\zeta < -0.5$) classes (Fig. 5) show clear transitions from a quasi-Gaussian regime at large lags ($\tau = 2$ in figure) to distributions with sharper peaks and longer tails at scales well within the inertial subrange ($\tau = 0.05$).

This behavior has been documented for a wide range of turbulent flows⁵⁵ and is associated with the build up of intermittency³² due to self-amplification inertial dynamics⁵⁶.

The bulk of the pdf of temperature increments at any given scale can also be characterized by the coefficients of Eq. (11). Results show some differences between runs with differing $|\zeta|$ (Fig. 6). Namely, for runs in the strongly unstable class, q_0 exhibits a more pronounced peak around the origin and is characterized by larger asymmetry at the cross-over scale $\tau = 1$ compared to their near-neutral counterparts (Fig. 6(A)). Moreover, the results here confirm that a choice of linear $r_0(\Delta T)$ and quadratic $q_0(\Delta T)$ appear reasonable for ASL flows. In the case of an unstable ASL, the term $r_0(\Delta T)$ remains linear, while inspection of $q_0(\Delta T)$ suggests that a dependence on s with an exponent smaller than 2 might be more appropriate, corresponding to stretched exponential tails for $p(\Delta T)$ for small lags τ in unstable ASL flows. Comparison with the same data after run-by-run spectral phase randomization⁵⁴ shows that the latter exhibits almost Gaussian behavior, supporting the hypothesis that the emergence of long tails at inertial scales is primarily a consequence of non linear structures in the original time series.

The rate of change of the tail parameters η and q (Fig. 8) with decreasing scale τ provides a robust measure of how the distributional tails of $p(\Delta T)$ evolve at the onset of the inertial range. Fig. 7 shows that at large scales - where the pdf closely resembles a Gaussian - both η and q do not exhibit a significant dependence on the stability regime. On the contrary, at small scales $\tau = 0.05$ the tail behavior of ΔT is clearly dependent on ζ , especially the left tail of the pdf. Moreover, the scalewise rate of change of η and q reflects this dependence of ζ , as shown in Fig. 8. This evidence suggests that the observed intermittency is not only internal (i.e., not only due to variability in the instantaneous dissipation rate⁹) but is also directly impacted by the larger scale eddy motion that sense boundary conditions. In particular, when buoyancy generation is significant, the heat flux $\overline{w'T'}$ is connected with the sweep and sudden ejection of air parcels, corresponding with the sharp edges of the temperature ramps^{2,13}. The resulting sawtooth behavior could be responsible for the injection of scalar variance at small scales (instead of a gradual cascade), acting in particular on the negative tail of the ΔT pdf, as evident from Fig. 6(A). On the other hand, the buildup of non-Gaussian statistics for velocity increments is not as impacted by the stability regime, and therefore the dominant effects are in this case primarily an effect of internal intermittency.

B. Probabilistic description of asymmetry across scales

The presence of a finite third order temperature structure function signifies that local isotropy is not fully attained in the range of scales explored here. The S_T^3 exhibits a plateau for scales smaller than I_w (Fig. 9(A)) similar to previous measurements reported in grid turbulence forced by a mean temperature gradient⁵⁷. Moreover, S_T^3 levels off to positive values for $\zeta > 0$, while it becomes negative for $\zeta < 0$. This finding is consistent with the presence of ramp-like structures when $\zeta > 0$ (mildly stable conditions) that are inverted when compared to their unstable counterparts.

The findings here confirm that at the cross-over from production to inertial, imprints of ramp structures persists well into the inertial subrange. The consequence of these imprints on time-reversibility is now considered for temperature sequences. The irreversibility analysis detects strong irreversibility at large scales that slowly decreases at the onset of the inertial range (Fig. 9). This finding is consistent with the idea that atmospheric stability determines a preferential direction for the large-scale scalar structures, which becomes progressively weaker at scales smaller than $\tau = 1$. Here the sign of the heat flux has a primary effect on the orientation of the ramps, as captured by R_τ . Furthermore, phase randomization is shown to destroy much of this time irreversibility (Fig. 9(B)) while the addition of synthetic ramps, either with positive or negative orientation, produces values of R_τ that closely resemble observations of stable and unstable ASL respectively. These synthetic experiments also recover the sign of the third order moment S_T^3 (Fig. 9(A)) but not its magnitude at smaller scales. As one would expect, a sawtooth time series does not fully reproduce inertial scale scalar dynamics, even though it does capture the effect of boundary conditions on scalar ramp-cliffs.

The averaged relative entropy $\langle Z_\tau \rangle$, while insensitive to the ramp orientation, at every given level T quantifies the imbalance between forward and backward probability fluxes of temperature trajectories (Fig. 10(A)). Again, irreversibility of scalar records increases with the lag τ and here tend to plateau at larger scales ($\tau > 1$).

Phase-randomized time series, by comparison, exhibit smaller values of $\langle Z_\tau \rangle$ in the inertial range. As one would expect, the excess is thus likely a direct result of the presence of scalar ramps. The presence of asymmetric patterns in temperature time traces further suggests that in the inertial range scalar turbulence is more time-irreversible than velocity, as confirmed

by the larger values of $\langle Z_\tau \rangle$ at inertial scales (Fig. 10(B)).

Time-irreversibility of phase space trajectories was further investigated by testing if a significant difference exists between the probability distribution $p(T'_\tau|T)$ and $p(-T'_\tau|T)$. To this end, a Kolmogorov-Smirnov (KS) test was performed at the significance level 0.05. At every scale τ , results were averaged over different values of T and across runs within the same stability class. The results from the KS test (Figure 10, panels (C) and (D)) confirm the picture obtained from the relative entropy measure $\langle Z_\tau \rangle$: The pdf of forward and backward temperature diverge significantly as the scale τ increases. While this test does not capture the sign of the ramps, the behavior of near neutral runs exhibit some difference from the case of relevant heat flux: near neutral runs appear on average more reversible than unstable runs at the same dimensionless scale τ .

DISCUSSION AND CONCLUSIONS

It is well known that in turbulence the pdfs of scalar increments develop heavier tails with decreasing scales in the inertial range when compared to their velocity counterparts. The analysis here documented shows that within the first two decades of the inertial subrange, this buildup of tails also carries the signature of turbulent kinetic energy generation. The direct injection of scalar variance from large scales seem to hinder any universal description of ΔT statistics within this range of scales. Instead, the pdf of $\Delta T(r)$ for ASL flows appear to be conditional on the value of ζ .

This dependence on atmospheric stability regimes observed for $p(\Delta T)$ further suggests that the topology of large eddies, and in particular the presence of ramp-cliff scalar structures, may be responsible for the scale-wise evolution of intermittency and the persistent time directionality at fine scales. This intermittency excess observed in the transition from production to inertial scales is consistent with self-amplification dynamics taking place that further excite the excess of scalar variance injected by the ramps.

However, while measures of intermittency appear to be dependent on the absolute value of ζ , i.e., on the relative magnitude of shear and buoyancy production terms (regardless on the sign of the heat flux), the analysis of asymmetry and time reversibility clearly sense the sign of the heat flux H more than the magnitude of ζ itself. This effect is arguably a product of the preferential orientation that the external temperature gradient imposes

on the scalar ramp-cliffs, as explained by sweep-ejection dynamics. This hypothesis was here further tested by comparisons with synthetic time series that mimic ramp-cliff patterns observed in the scalar time series. The analysis confirmed that much of the observed time irreversibility, as well as its dependence on the sign of H , are recovered by these surrogate time series (Fig. 9).

Our analysis of time directional properties showed that time-irreversible behavior for the scalar is stronger at the large scales of the flow where boundary conditions, and in particular the sign of H , determine the orientation and structure of the eddies. At finer scales, time irreversibility as quantified by both $\langle Z_\tau \rangle$ and R_τ progressively decreases as advection destroys the preferential eddy orientation imposed by boundary conditions. Note that this behavior is not captured by a simple measure of skewness such as S_T^3 (Fig. 9(A)), which is small at large scales and plateaus in the inertial range consistent with previous experiments⁴ and numerical simulations⁵⁸, thus showing that local isotropy is not fully attained at the finer scales examined here.

Turbulent flows exist in a state far from thermodynamic equilibrium, with the flow statistics exhibit irreversibility. This irreversibility is typically described in terms of fluxes of energy or asymmetries in the pdfs of the fluid velocity increments⁵⁹. Similar methods could be used to describe irreversibility in the scalar field, e.g. using S_T^3 , and this would imply that the irreversibility of the scalar field is stronger at smaller scales than it is at larger scales. However, in this paper we have used alternative measures to quantify the irreversibility, namely $\langle Z_\tau \rangle$ and R_τ . These quantities paint a different picture, namely that it is the largest scales, not the smallest scales in the scalar field that exhibit the strongest irreversibility. A potential cause for these differing behaviors is that whereas fluxes and quantities such as S_T^3 are multi-point, single-time quantities, $\langle Z_\tau \rangle$ and R_τ are single-point, multi-time quantities. Thus, these two ways of describing irreversibility can tell us fundamentally different things about the nature of irreversibility in turbulence, which involves fields that evolve in both space and time. This is something that we shall explore in future work.

Collectively, the results presented in this paper suggest the following picture for ASL turbulence at the cross-over from production to inertial. Increasing instability in the ASL leads to increases in the mean turbulent kinetic energy dissipation rate (as evidenced by Eq. (1)) and its spatial autocorrelation function and pdf. The consequences of this increased dissipation with increased instability has different outcomes for velocity and scalar turbu-

lence. For velocity, refinements to K41 appear sufficient to explain the observed scaling. For scalar turbulence, the picture appears far more complicated. Intermittency buildup at inertial scales is more rapid when compared to their velocity counterparts, and the signature of the temperature variance injection mechanism persists at even the finer scales explored here.

Turbulence and scalar turbulence are characterized by a constant flux of energy and scalar variance from the scales of production down to dissipation. While early theories hypothesized a cascade only depending on these quantities, experimental evidence to date supports a more complicated picture. The multi-time information encoded in $\langle Z_\tau \rangle$ reveal that time-reversibility is not constant across scales, as do the fluxes of information entropy. Probability fluxes forward and backward in time are not balanced in general for air temperature increments, especially at the cross-over from production to inertial. Furthermore, these fluxes carry the signature of the external boundary conditions and show that dissipation rates themselves are not independent of the large-scale dynamics. Although a formal analogy between Eq. (15) and the thermodynamics of microscopic non-equilibrium steady state systems exists, we stress that in the present application turbulent fluctuations are macroscopic and are the result of non-linear and non-local interactions.

ACKNOWLEDGMENTS

E.Z. acknowledges support from the Division of Earth and Ocean Sciences, the Nicholas School of the Environment at Duke University. G.K. acknowledges support from the National Science Foundation (NSF-EAR-1344703, NSF-AGS-1644382, and NSF-DGE-1068871) and from the Department of Energy (DE-SC0011461). Helpful discussions with Marco Marani, Brad Murray and Amilcare Porporato are gratefully acknowledged.

DISCLAIMER

The authors declare no conflict of interest.

REFERENCES

- ¹K. R. Sreenivasan, Reviews of Modern Physics **71**, S383 (1999).

- ²R. Antonia, A. Chambers, C. Friehe, and C. Van Atta, *Journal of the Atmospheric Sciences* **36**, 99 (1979).
- ³B. I. Shraiman and E. D. Siggia, *Nature* **405**, 639 (2000).
- ⁴Z. Warhaft, *Annual Review of Fluid Mechanics* **32**, 203 (2000).
- ⁵J. R. Garratt, *Earth-Science Reviews* **37**, 89 (1994).
- ⁶R. B. Stull, *An Introduction to Boundary Layer Meteorology*, Vol. 13 (Springer Science & Business Media, 2012).
- ⁷A. N. Kolmogorov, in *Dokl. Akad. Nauk SSSR*, Vol. 30 (JSTOR, 1941) pp. 301–305.
- ⁸R. H. Kraichnan, *The Physics of Fluids* **11**, 945 (1968).
- ⁹V. Kuznetsov, A. Praskovsky, and V. Sabelnikov, *Journal of Fluid Mechanics* **243**, 595 (1992).
- ¹⁰J. Schumacher, J. D. Scheel, D. Krasnov, D. A. Donzis, V. Yakhot, and K. R. Sreenivasan, *Proceedings of the National Academy of Sciences* **111**, 10961 (2014).
- ¹¹P. Yeung, X. Zhai, and K. R. Sreenivasan, *Proceedings of the National Academy of Sciences* **112**, 12633 (2015).
- ¹²G. G. Katul, C. Manes, A. Porporato, E. Bou-Zeid, and M. Chamecki, *Physical Review E* **92**, 033009 (2015).
- ¹³G. Katul, A. Porporato, D. Cava, and M. Siqueira, *Physica D: Nonlinear Phenomena* **215**, 117 (2006).
- ¹⁴A. Reynolds, *Physica A: Statistical Mechanics and its Applications* **391**, 5059 (2012).
- ¹⁵H. Xu, A. Pumir, G. Falkovich, E. Bodenschatz, M. Shats, H. Xia, N. Francois, and G. Boffetta, *Proceedings of the National Academy of Sciences* **111**, 7558 (2014).
- ¹⁶G. Falkovich, K. Gawdzki, and M. Vergassola, *Reviews of Modern Physics* **73**, 913 (2001).
- ¹⁷C. Meneveau, T. S. Lund, and W. H. Cabot, *Journal of Fluid Mechanics* **319**, 353 (1996).
- ¹⁸F. Porté-Agel, C. Meneveau, and M. B. Parlange, *Journal of Fluid Mechanics* **415**, 261 (2000).
- ¹⁹C. W. Higgins, M. B. Parlange, and C. Meneveau, *Boundary-Layer Meteorology* **109**, 59 (2003).
- ²⁰R. Stoll and F. Porté-Agel, *Water Resources Research* **42** (2006).
- ²¹G. G. Katul, A. G. Konings, and A. Porporato, *Physical Review Letters* **107**, 268502 (2011).
- ²²G. G. Katul, D. Li, M. Chamecki, and E. Bou-Zeid, *Physical Review E* **87**, 023004 (2013).

- ²³D. Li, G. G. Katul, and E. Bou-Zeid, *Physics of Fluids* **24**, 105105 (2012).
- ²⁴G. G. Katul, A. Porporato, S. Shah, and E. Bou-Zeid, *Physical Review E* **89**, 023007 (2014).
- ²⁵D. Li, G. G. Katul, and S. S. Zilitinkevich, *Journal of the Atmospheric Sciences* **72**, 2394 (2015).
- ²⁶A. Monin and A. Obukhov, *Contrib. Geophys. Inst. Acad. Sci. USSR* **151**, e187 (1954).
- ²⁷W. Chen, M. D. Novak, T. A. Black, and X. Lee, *Boundary-Layer Meteorology* **84**, 99 (1997).
- ²⁸C. Thomas and T. Foken, *Boundary-Layer Meteorology* **122**, 123 (2007).
- ²⁹G. Katul, C.-I. Hsieh, and J. Sigmon, *Boundary-Layer Meteorology* **82**, 49 (1997).
- ³⁰A. Obukhov, in *Dokl. Akad. Nauk. SSSR*, Vol. 67 (1949) pp. 643–646.
- ³¹K. Sreenivasan, in *Proceedings of the Royal Society of London A: Mathematical, Physical and Engineering Sciences*, Vol. 434 (The Royal Society, 1991) pp. 165–182.
- ³²A. N. Kolmogorov, *Journal of Fluid Mechanics* **13**, 82 (1962).
- ³³G. G. Katul, M. B. Parlange, and C. R. Chu, *Physics of Fluids* **6**, 2480 (1994).
- ³⁴G. Katul, B. Vidakovic, and J. Albertson, *Physics of Fluids* **13**, 241 (2001).
- ³⁵S. Pope and E. S. Ching, *Physics of Fluids A: Fluid Dynamics* **5**, 1529 (1993).
- ³⁶Y. G. Sinai and V. Yakhot, *Physical Review Letters* **63**, 1962 (1989).
- ³⁷E. S. Ching, *Physical Review Letters* **70**, 283 (1993).
- ³⁸C. W. Gardiner, *Handbook of Stochastic Methods* (Springer-Verlag, Berlin–Heidelberg–New York–Tokyo, 1985, p.124).
- ³⁹A. Porporato, P. Kramer, M. Cassiani, E. Daly, and J. Mattingly, *Physical Review E* **84**, 041142 (2011).
- ⁴⁰U. Frisch and D. Sornette, *Journal de Physique I* **7**, 1155 (1997).
- ⁴¹C. Tsallis, *Journal of Statistical Physics* **52**, 479 (1988).
- ⁴²C. Tsallis, S. V. Levy, A. M. Souza, and R. Maynard, *Physical Review Letters* **75**, 3589 (1995).
- ⁴³B. Shi, B. Vidakovic, G. G. Katul, and J. D. Albertson, *Physics of Fluids* **17**, 055104 (2005).
- ⁴⁴T. Gotoh and R. H. Kraichnan, *Physica D: Nonlinear Phenomena* **193**, 231 (2004).
- ⁴⁵F. Ramos, C. R. Neto, and R. Rosa, arXiv preprint cond-mat/0010435 (2000).

- ⁴⁶F. M. Ramos, R. R. Rosa, C. R. Neto, M. J. Bolzan, L. D. A. Sá, and H. F. C. Velho, *Physica A: Statistical Mechanics and its Applications* **295**, 250 (2001).
- ⁴⁷T. Arimitsu and N. Arimitsu, *Chaos, Solitons & Fractals* **13**, 479 (2002).
- ⁴⁸M. J. Bolzan, F. M. Ramos, L. D. Sá, C. Rodrigues Neto, and R. R. Rosa, *Journal of Geophysical Research: Atmospheres* **107** (2002).
- ⁴⁹A. Lawrance, *International Statistical Review/Revue Internationale de Statistique* , 67 (1991).
- ⁵⁰T. M. Cover and J. A. Thomas, *Elements of Information Theory* (John Wiley & Sons, 2012, p.18).
- ⁵¹A. Porporato, J. Rigby, and E. Daly, *Physical Review Letters* **98**, 094101 (2007).
- ⁵²G. I. Taylor, in *Proceedings of the Royal Society of London A: Mathematical, Physical and Engineering Sciences*, Vol. 164 (The Royal Society, 1938) pp. 476–490.
- ⁵³R. H. Kraichnan, *Physical Review Letters* **72**, 1016 (1994).
- ⁵⁴D. Prichard and J. Theiler, *Physical Review Letters* **73**, 951 (1994).
- ⁵⁵C. Meneveau, *Journal of Fluid Mechanics* **232**, 469 (1991).
- ⁵⁶Y. Li and C. Meneveau, *Physical Review Letters* **95**, 164502 (2005).
- ⁵⁷L. Mydlarski and Z. Warhaft, *Journal of Fluid Mechanics* **358**, 135 (1998).
- ⁵⁸A. Celani, A. Lanotte, A. Mazzino, and M. Vergassola, *Physical Review Letters* **84**, 2385 (2000).
- ⁵⁹G. Falkovich, *Journal of Physics A: Mathematical and Theoretical* **42**, 123001 (2009).
- ⁶⁰R. Antonia, E. Hopfinger, Y. Gagne, and F. Anselmet, *Physical Review A* **30**, 2704 (1984).
- ⁶¹C. Meneveau, K. Sreenivasan, P. Kailasnath, and M. Fan, *Physical Review A* **41**, 894 (1990).
- ⁶²G. Ruiz-Chavarria, C. Baudet, and S. Ciliberto, *Physica D: Nonlinear Phenomena* **99**, 369 (1996).

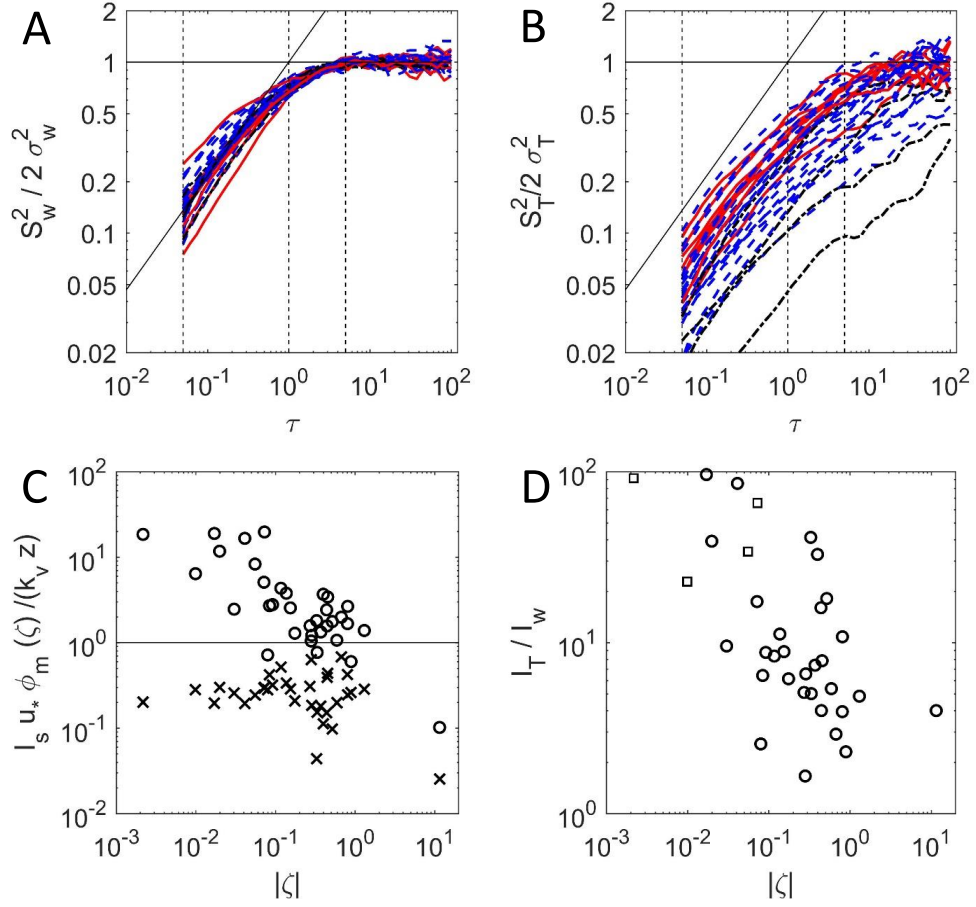


FIG. 1. In the upper panels, the normalized second order structure functions for vertical velocity (A) and temperature (B) are shown for runs that are weakly unstable (blue dashed lines), strongly unstable (red lines), and stable (black dash-dot lines). Black lines indicate the value 1 and the $2/3$ power law for reference; vertical dashed lines correspond to the dimensionless scales $\tau = 0.05$ (smallest scale not impacted by instrument path length), $\tau = 1$ (integral scale of the flow), and $\tau = 5$ (typical scale larger than I_w , while small enough not to be impacted by statistical convergence issues in structure functions calculations). Upper panels illustrate (C) the integral scales of the flow for $s = T$ (circles) and $s = w$ (crosses) as a function of the stability parameter $|\zeta|$, and (D) their ratio I_T to I_w again as a function of $|\zeta|$, where stable runs ($\zeta > 0$) are indicated by black squares.

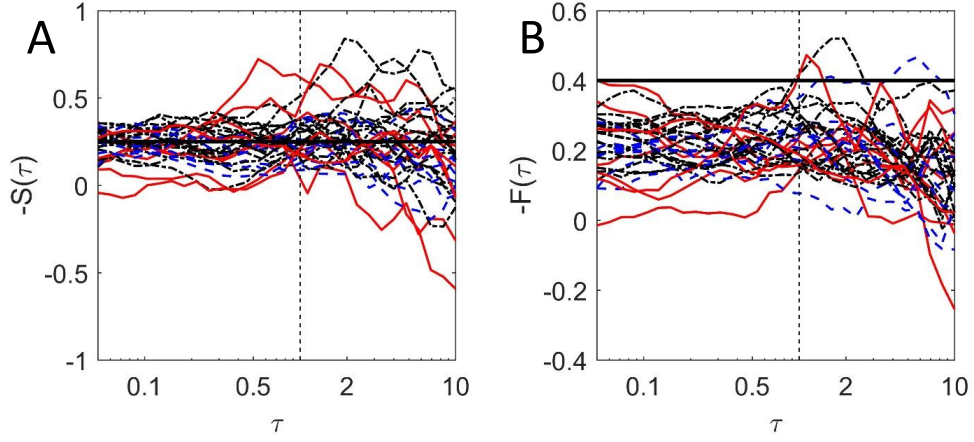


FIG. 2. Normalized third order structure functions $S(\tau)$ and $F(\tau)$ at the crossover from inertial to production scales. Vertical dashed line indicates the integral time scales, horizontal lines show the constant values 0.25 (A) and 0.4 (B). Results are shown for weakly unstable runs (blue dashed lines), strongly unstable (red lines), and stable runs (black dash-dot lines).

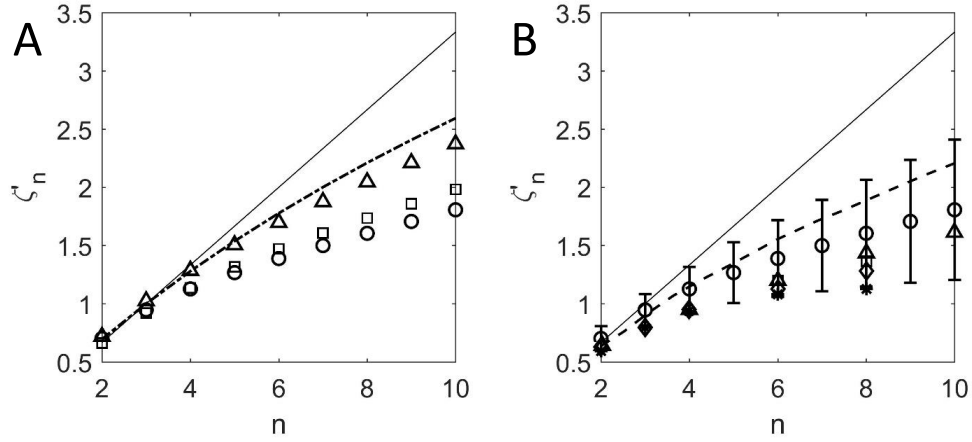


FIG. 3. (A) Average values of the scaling exponents for longitudinal velocity u (triangles), vertical velocity w (squares), and temperature T (circles). Black continuous line and dashed line show respectively the K41 and the She-Leveque predictions for the longitudinal velocity structure functions. Exponents are computed from scales ranging between $\tau = 0.05$ and $\tau = 0.2$. (B) Scaling exponents for temperature; Mean and standard deviation values are computed over all the runs and are indicated by circles and vertical bars, respectively. Data from Mydlarsky and Warhaft (1990)⁵⁷ (squares), Antonia et al. (1984)⁶⁰ (triangles), Meneveau et al. (1990)⁶¹ (*) and Ruiz et al. (1996) (diamonds)⁶² are shown for comparison. The KOC scaling (black line) and results from the Kraichnan model (1994)⁵³ (dashed line) as reported in⁴ are also presented for reference.

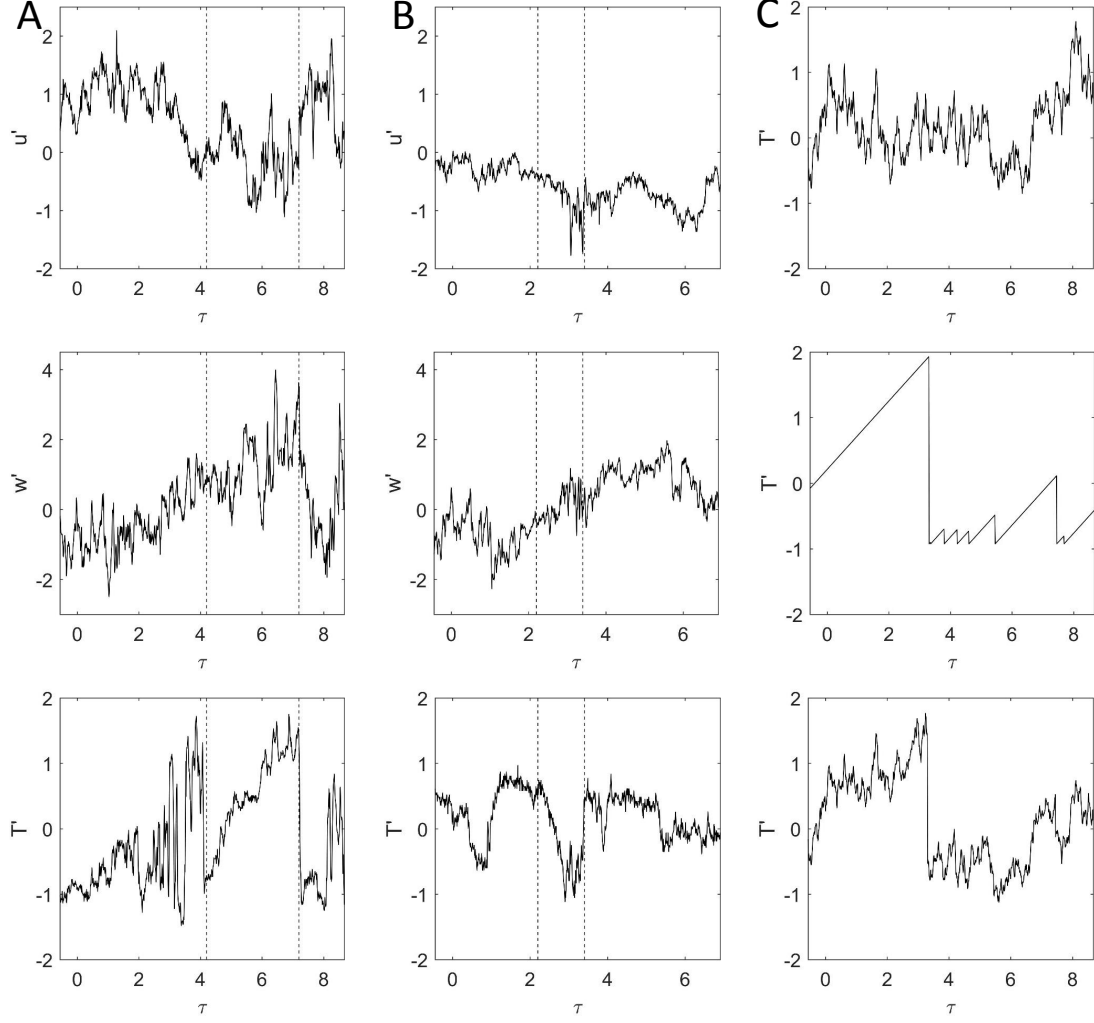


FIG. 4. Sequences of velocity and temperature fluctuations extracted from an unstable run (run 34, $\zeta = -0.52$, $I_w = 1.74s$, column A) and a stable/near neutral one (run 27, $\zeta = 0.073$, $I_w = 2.18s$ column B). The presence of ramps and inverted-ramp like structures respectively is marked by dashed vertical lines. Column (C) shows a phase-randomized sequence obtained from run 34 (top), a series of synthetic ramps with durations exponentially distributed with mean $2I_w$ (middle) and the surrogate time series obtained merging the above sawtooth pattern with the phase randomized time series (bottom), where the relative weight of the ramps α was set equal to 0.5.

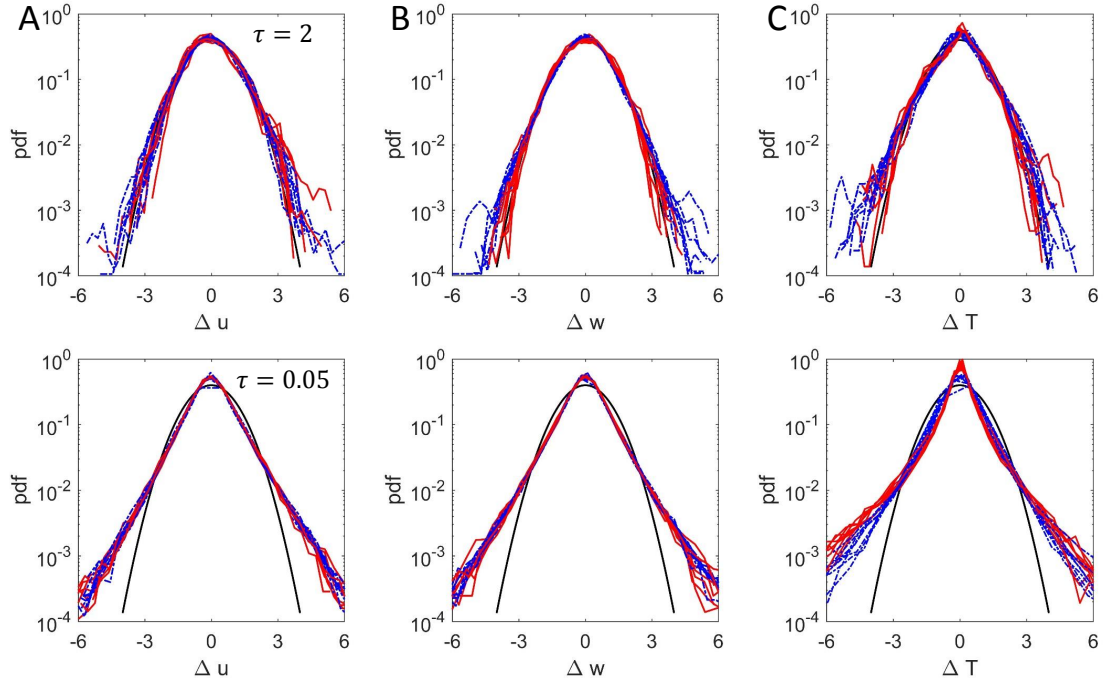


FIG. 5. Normalized probability density functions observed for increments of longitudinal velocity (A), vertical velocity (B) and air temperature (C) at large scales ($\tau = 2$, top row) and small scales ($\tau = 0.05$, bottom). The figure includes data for runs in the strongly unstable class ($\zeta < -0.5$), and near neutral class ($|\zeta| < 0.072$). Black lines show the standard Gaussian distribution for reference.

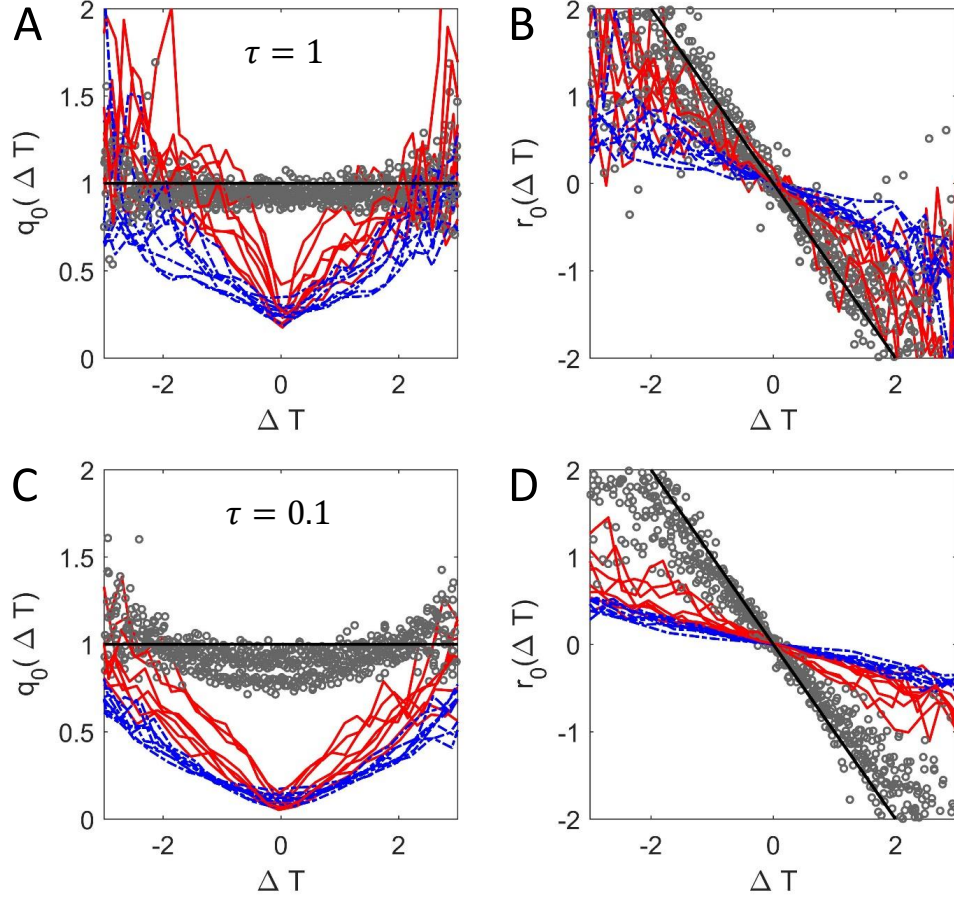


FIG. 6. Functions $q_0(\Delta T)$ and $r_0(\Delta T)$ estimated from the conditional derivatives of the original runs, for the two classes of strongly unstable (red lines) and near neutral runs (blue dotted lines). The same quantities are reported for phase-randomized surrogate time series for comparison (grey circles). Results are shown only for the central body of the pdf (within 3σ from the mean) for illustration purposes. Top panels (A,B) are computed for a lag equal to the integral time scale of the flow $\tau = 1$, while the bottom panels (C,D) correspond to the smaller time lag $\tau = 0.1$. Black lines $q_0 = 1$ and $r_0 = -\Delta T$ correspond to the Gaussian distribution.

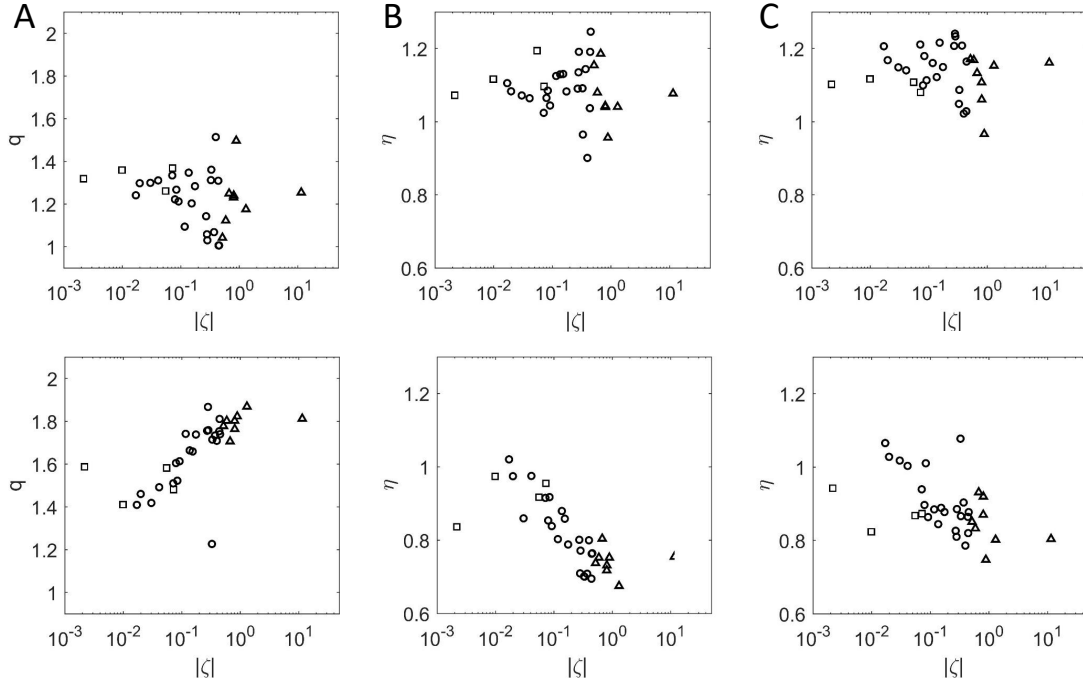


FIG. 7. Tail parameters q and η as a function of the atmospheric stability parameter ζ . Results include the Q-Gaussian parameter q (A) and the stretched exponential shape parameter η , obtained from fitting the left (B) and right tail (C) of the distribution $p(\Delta T)$. Values of q and η are reported for large scales ($\tau = 5$, upper panels) and small scales ($\tau = 0.05$, lower panels). Triangles denote strongly unstable runs ($\zeta < -0.5$), squares denote stable runs ($\zeta > 0$) and circles refer to slightly unstable runs ($-0.5 < \zeta < 0$).

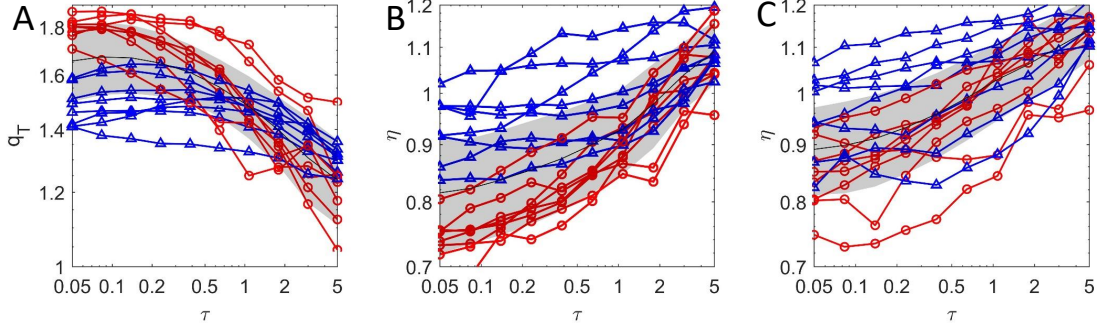


FIG. 8. Evolution of the tail parameter q for the assumed q-Gaussian model (A), and for the stretched exponential shape parameter η from separate fit to the left (B) and right (C) tails of the distribution of temperature increments across scales τ . Data from two stability classes are included: strongly unstable ($\zeta < -0.5$, red circles) and near neutral conditions ($|\zeta| < 0.072$, blue dashed lines). Black lines and shaded areas indicate average and standard deviation respectively computed over all the runs in our dataset.

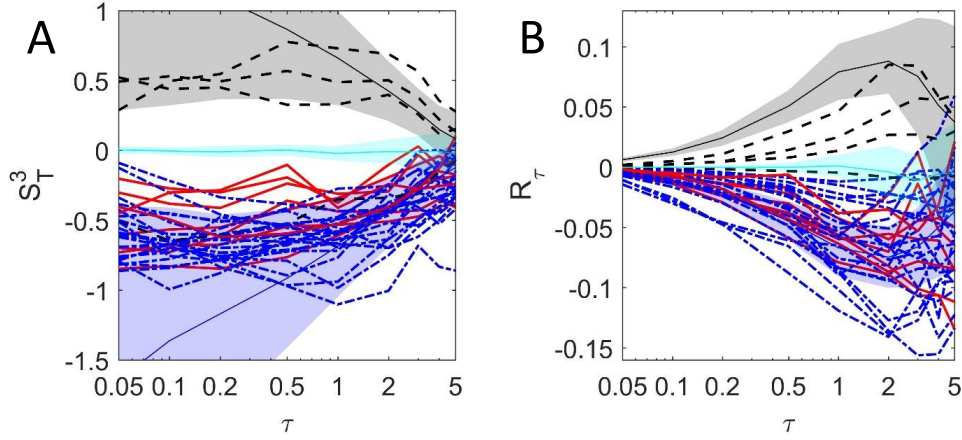


FIG. 9. Measures of asymmetry S_T^3 (A) and time irreversibility R_τ (B) computed for temperature increments for scales varying from $\tau = 0.05$ to $\tau = 5$. The plots include stable runs (black dashed lines), weakly unstable runs (blue dash-dot lines) and strongly unstable runs (red lines). For reference, the same quantities are computed for phase-randomized time series (cyan), and sythetic time series with sawtooth positive (blue) and inverted ramps (black). Shaded regions correspond to the 1σ -confidence intervals over 34 realizations of the surrogate time series. Here weight and mean duration of the ramps were set to $\alpha = 0.4$ and $2I_w$ respectively.

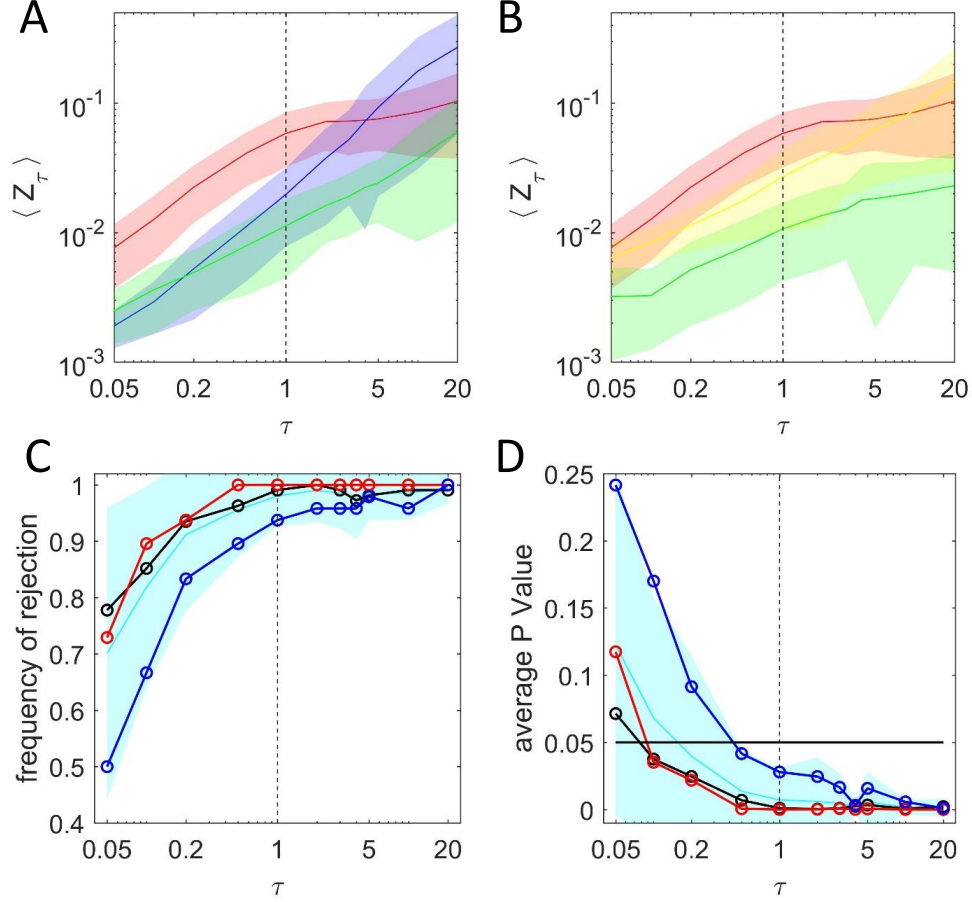


FIG. 10. (A) Mean and standard deviation over 34 time series of $\langle Z_\tau \rangle$ computed for scales varying from $\tau = 0.05$ to $\tau = 5$. Values of $\langle Z_\tau \rangle$ are shown for original temperature records (red), and surrogate time series obtained by phase-randomization (green). For comparison, the same analysis is reported for fractional brownian motion with Hurst exponent $H = 1/3$ (blue). (B) A comparison of $\langle Z_\tau \rangle$ for temperature (red), longitudinal velocity (yellow) and vertical velocity (green). Lower panel report the Kolmogorov-Smirnov test average rejection rate (C) and average P-value (D) computed for all the temperature time series (cyan for mean value and 1σ confidence interval), and for different stability classes: strongly unstable runs ($\zeta < -0.5$, red), near-neutral runs ($\zeta < -0.5$, blue) and intermediate values ($0.072 < |\zeta| < 0.5$, black). KS test was performed at the 0.05 significance level, corresponding to the horizontal line in (D). The vertical dashed line marks the integral time scale I_w .